THE JOURNAL OF PHYSICAL CHEMISTRY C
A JOURNAL OF THE AMERICAN CHEMICAL SOCIETY

pubs.acs.org/JPCC

Article

Highly Luminescent NHC-Stabilized Au_{13} Clusters as Efficient Excited-State Electron Donors

Xiaotong Wang, Rong Liu, Limei Tian, Jingwen Bao, Chunyi Zhao, Fushuang Niu, Dajiao Cheng, Zhou Lu, and Ke Hu*

Cite This: *J. Phys. Chem. C* 2022, 126, 18374−18382

Read Online

ACCESS | Metrics & More | Article Recommendations | Supporting Information

ABSTRACT: Atomically precise *N*-heterocyclic carbene (NHC)-stabilized gold nanoclusters (Au NCs) have attracted great attention among a variety of gold nanoclusters. Herein, a series of three NHC-stabilized Au_{13} NCs have been synthesized featuring ligands with different steric hindrances. Their electrochemical and photophysical properties were investigated. The bidentate NHC ligands with pendant pyrenes rendered the most sterically hindered Au_{13} NC, $[Au_{13}(bis\text{-}NHC^{Pyr})_5Cl_2]^{3+}$, highly luminescent (quantum yield, 56%) and long-lived (3.4 μs, dichloromethane) among the three Au_{13} NCs. The excellent photoluminescence properties were attributed to the suppression of excited-state vibrational relaxation arising from the cluster structural rigidity. Further transient spectroscopic investigation of the Au NC excited state also showed favorable electron transfer to methyl viologen with the highest quantum yield from $[Au_{13}(bis\text{-}NHC^{Pyr})_5Cl_2]^{3+}$ (Φ_{e-T}, 12%). Understanding the relationship between the excited-state behavior and the sterically hindered structure of NHC-ligated Au NCs will assist in better designing NHC-stabilized Au NCs as photosensitizers for applications in organic photoredox catalysis, sensors, and solar energy conversion.

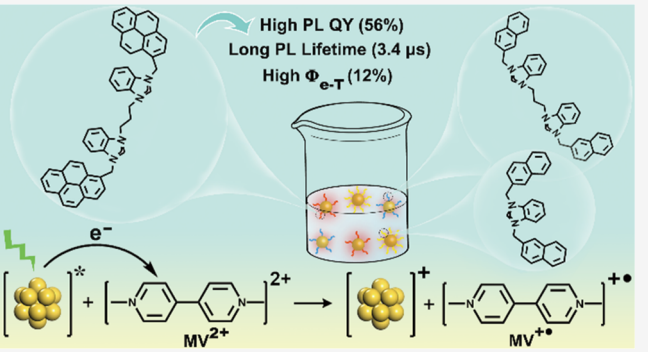

INTRODUCTION

Ligand-protected gold nanoclusters have been widely studied in recent years owing to their atomically precise structures, quantum confinement effects, and easily tunable photophysical properties. They have been used in a wide range of applications in catalysis, biological sensors, and solar cells.[1−4] Studies on ligand-protected gold nanoclusters can be traced back to the 1960s when phosphine-modified gold nanoclusters were first synthesized.[5,6] Since then, ligand-protected gold nanoclusters have developed rapidly. So far, studies on ligands for atomically precise gold nanoclusters have been mainly about thiolates, phosphines, and alkynyls.[7−13] However, these ligands were often labile and prone to dissociation or ligand exchange, decreasing the stability of gold nanoclusters, which limited the applications of gold nanoclusters as photocatalysts that required long-term turnovers.[1,13,14] Therefore, searching for strong and stable binding ligands was crucial for the development of ligand-protected gold nanoclusters. Recently emerging *N*-heterocyclic carbene (NHC) ligands are potent σ donors and able to form strong C−M bonds with most metallic materials.[15,16] Theoretical calculations also implied that bulky NHC could form the strongest covalent bond to Au NCs by comparing with the widely used thiolates, phosphines, and alkynyl ligands.[17,18] Therefore, the NHC-protected gold nanoclusters (Au NCs) have exhibited excellent stability based on the strong C−Au bond as well as the multiple $\pi-\pi$ and CH−π interactions.[19−22]

Besides stability, long-lived excited states of photocatalysts are also essential for diffusional encounters of redox substrates in photoredox catalysis. The photoluminescence quantum yield (PLQY) is a good figure of merit to optimize to make gold nanoclusters good photosensitizers or photocatalysts. NHC-stabilized gold nanoclusters generally reported a relatively high PLQY (>10%).[20,21,23−25] Crudden's group was the first to report gold nanoclusters with monodentate NHC ligands with up to 16% PLQY.[20] Zheng's group unveiled the synthesis of Au_{13} NCs protected by bis-*N*-heterocyclic carbene (bis-NHC) ligands with an observed high PLQY (14.99%) and a long lifetime (2.4 μs).[21] Zang and his team adjusted N-substituents to obtain nonemissive Au_{11} and emissive Au_{13} NCs (QY = 16%).[23] Recently, Crudden's group further extended the QY to 23% by enantioseparation of chiral bis-NHC-stabilized Au_{13} NCs.[24] To further increase the PLQY of

Received: September 6, 2022
Revised: October 8, 2022
Published: October 21, 2022

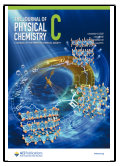

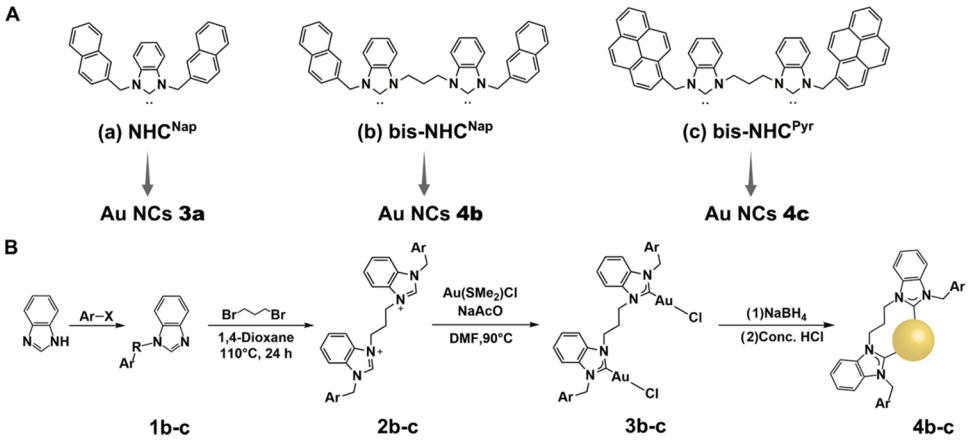

Figure 1. (A) Molecular structures of NHC ligands (a–c) used in this work. (B) Synthesis of NHC-stabilized Au_{13} clusters based on different bis-NHC ligands.

NHC-protected Au NCs, herein, we explored a new Au NC design method with a series of NHC ligands that varied both in the chelating number (monodentate vs bidentate) and the steric hindrance of the ligands. New NHC ligands with naphthalene (Nap) and pyrene (Pyr) peripheral groups were incorporated as steric factors. Bidentate NHCs with bulky Pyr were found to stabilize the gold cluster core and suppress the excited-state nonradiative relaxation. Impressively, the bis-NHC with the N-wingtip of pyrene-stabilized Au NCs (Au bis-NHC^{Pyr} NCs) showed a photoluminescence quantum yield as high as 56% and a photoluminescence lifetime over 3 μs. The excited-state electron transfer properties of NHC-protected Au NCs were studied through photoreduction of methyl viologen (MV^{2+}) using transient absorption spectroscopy. The relationship between the excited-state behavior and the sterically hindered structure of NHC-ligated Au NCs was revealed.

EXPERIMENTAL SECTION

Materials. All chemicals were purchased from Adamas or Beijing Innochem Science & Technology Co., Ltd. and were used without further purification.

Instruments. The absorption spectra were recorded on an Agilent Cary 60 UV–vis spectrometer. The measurement of the quantum yield was performed on an Edinburgh FLS1000, and other steady-state photoluminescence spectra were recorded on an Agilent Cary Eclipse fluorimeter. ^{1}H NMR spectra were recorded on a Bruker AVANCE III HD-400 MHz spectrometer. The high-resolution transmission electron microscopy (HR-TEM) image was taken on a Tecnai G2 F20 S-Twin. ESI-MS spectra were recorded on a McriO-TOF11 mass spectrometer in dichloromethane/acetonitrile (v/v = 1:1) solutions, and the simulated spectrum isotopic distribution patterns were obtained from the software Isopro 3.0.

Femtosecond Transient Absorption Spectroscopy. The femtosecond transient absorption (fs-TA) spectra were acquired with a UV–vis pump supercontinuum probe apparatus, which has been described in detail somewhere else.[26,27] In brief, a Ti:sapphire laser amplification system (Spitfire Ace, Spectra Physics) running in the 1 kHz mode was used to generate the 800 nm laser pulses with a pulse width of 80 fs and pulse energy of 6 mJ/pulse. A part of the laser output was led into an optical parametric amplification system (TOPAS Prime, Light Conversion) to generate the pump beam with tunable wavelength, which then passed through an optical chopper synchronized with the laser and running at 500 Hz before entering the sample cell. Another part of the laser beam was focused on a CaF_2 crystal to generate the white light continuum to serve as the probe light source. In this work, the samples were uniformly distributed in acetonitrile (spectroscopically pure grade) at a concentration of 2 mg/mL in a 1 mm long optical cell. The pump and probe beams overlapped at the sample cells, with their relative time of arrival controlled by an optical delay line. The overall time resolution of the TA measurement is about 150 fs. All of the samples were excited using 500 nm (20 μW) and probed with a white light continuum ranging between 350 and 700 nm. The signals were collected in transmission geometry.

Nanosecond Transient Absorption Spectroscopy. The nanosecond transient absorption spectra (ns-TA) were collected on a TSP-2000 (Unisoku) laser flash photolysis system as was previously described.[28] Briefly, different single-wavelength laser pulses (5–8 nm full width at half-maximum, 3 mJ/cm^2 per pulse) were output by the excitation source, a Q-switched frequency-doubled pulsed Nd/YAG laser (Quantel Q-Smart 450, 10 Hz). A 75 W xenon arc lamp was used as the probe beam and focused on the sample in a cuvette with a width of 1 cm. The probe beam was aligned orthogonally to the laser pulse of the excitation source, and then the detection of the signal was performed by an f/4 monochromator (Acton, Princeton Instrument), which was coupled to an R2949 photomultiplier tube (Hamamatsu). The computer-interfaced digital oscilloscope (LeCroy 4024, 12 bit, 200 MHz) showed transient absorption kinetics data with typical 50 laser pulse averages at each wavelength. To acquire transient photoluminescence data, the white light probe beam needed to be occluded, and only the laser pulse was used to excite the sample. The detection of signals was carried out in the same way as mentioned above. All nanosecond transient absorption spectroscopy measurements were performed at room temperature, and the samples were deaerated by N_2. Data were processed in Origin 9, and the least-squares error minimization was performed using the Levenberg–Marquardt iterative method.

Synthesis of NHC-Stabilized Au NCs. Three NHC-stabilized Au NCs **3a**, **4b**, and **4c** were prepared using 1,3-di(naphthalen-2-ylmethyl)benzimidazolin-2-ylidene (NHC^{Nap}), bidentate carbene ligand 1,3-bis(1-(naphthalen-2-

https://doi.org/10.1021/acs.jpcc.2c06370
J. Phys. Chem. C 2022, 126, 18374–18382

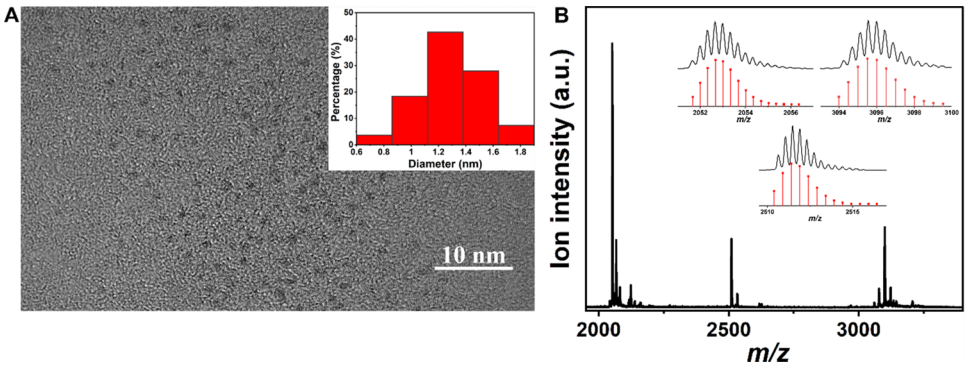

Figure 2. (A) HR-TEM images of **4c** (scale bar = 10 nm). Insets: Size distribution of **4c**. (B) ESI-MS spectrum of **4c** dissolved in dichloromethane (DCM). Inset: Experimental (black trace) and simulated (red trace) isotopic distribution of $[Au_{13}(bis\text{-}NHC^{Pyr})_5Cl_2]^{3+}$.

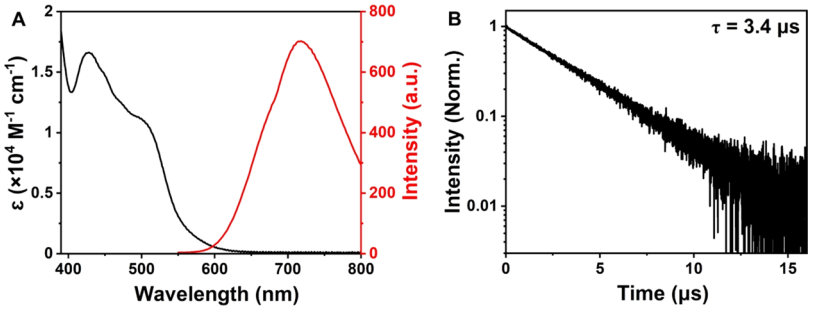

Figure 3. (A) UV−vis (black) and PL (red) spectra of **4c**. (B) Time-resolved PL decay of **4c** in DCM (λ_{ex} = 490 nm).

ylmethyl)-1H-benzimidazol-1-ium-3-yl) propane (bis-NHC^{Nap}), and 1,3-bis(1-(pyren-1-ylmethyl)-1H-benzimidazol-1-ium-3-yl) propane (bis-NHC^{Pyr}), respectively (Figure 1A). The mono-NHC Au NCs were synthesized according to reported literature procedures with appropriate modifications.[20] The bis-NHC Au NCs were synthesized as presented in Figure 1B. First, the benzimidazole reacted with corresponding haloalkanes via two-step nucleophilic substitutions to obtain corresponding benzimidazole salts. Second, the gold precursors NHC−Au−X (X = Cl, Br) were prepared by reactions between benzimidazole salts and $Au(SMe_2)Cl$ in the presence of the basic salt. Finally, the precursors were reduced by $NaBH_4$, followed by the addition of concentrated HCl to etch larger Au NCs, yielding the atomically precise Au_{13} NCs.[29]

Quantum Yield Measurement. The photoluminescence quantum yield was measured according to previous literature.[30−34] The samples to be tested, **3a**, **4b**, and **4c**, were dissolved in dichloromethane (DCM), and zinc phthalocyanine (ZnPc) dissolved in pyridine was used as the standard. They were placed in quartz cuvettes with a 1 cm optical path, sealed by rubber stoppers and parafilm, and purged with N_2 for 20 min to remove air. The sample and standard solutions had equal absorbance (around 0.05) at the excitation wavelength of 400 nm after purging with N_2. The area under each emission curve was integrated using Origin 9. The photoluminescence quantum yield of **3a**, **4b**, and **4c** were calculated by eq 1.

$$\Phi_F = (A_{std}/A)(F/F_{std})(n/n_{std})^2\Phi_{F(std)} \quad (1)$$

where F and F_{std} are the areas of the fluorescence emission curve of the sample and ZnPc, respectively, A and A_{std} are the absorbance of the sample and ZnPc at the excitation wavelength, respectively, and n and n_{std} are the refractive indices of the solvent used for the sample and ZnPc, respectively. The refractive indices of the solvents at room temperature are $n_{pyridine}$ = 1.5095 and n_{DCM} = 1.4242,[35] respectively. The quantum yield of standard ZnPc in pyridine ($\Phi_{F(std)}$) is 0.30.[36]

Photoluminescence Quenching. Generally, 2 mL of Au NC acetonitrile solutions with different concentrations of MV^{2+} were added into 1 cm path-length quartz cuvettes sealed by rubber stoppers and parafilm and purged with N_2 for 20 min. Then, the time-resolved photoluminescence decay of the mixture of Au NCs and MV^{2+} was recorded immediately at the probe wavelength of 710 nm after 490 nm pulsed laser excitation.

RESULTS AND DISCUSSION

The high-resolution transmission electron microscopy (HR-TEM) image of **4c** revealed the presence of well-dispersed Au NCs with an average diameter of about 1.3 nm (Figure 2A). The molecular formula of **4c** was confirmed by ESI-MS (Figure 2B), which demonstrated a main molecular ion peak at 2051.7 m/z, corresponding to $[Au_{13}(bis\text{-}NHC^{Pyr})_5Cl_2]^{3+}$. A minor peak at 3095.4 m/z was also distinguished, corresponding to the divalent ion $[Au_{13}(bis\text{-}NHC^{Pyr})_5Cl_2]^{3+}$ (Cl^-). Another peak at 2510.4 m/z, corresponding to $[Au_{11}(bis\text{-}NHC^{Pyr})_4Cl]^{2+}$, was derived from incomplete ionization of the parent cluster. The experimental results matched well with the simulated isotopic distribution patterns. The results manifested that **4c** has been successfully synthesized. The molecular formulas of **3a** and **4b** were confirmed by similar methods and are summarized in Table S1. The ^1H NMR characterization is shown in Figure S1. Single-crystal growth was not successful for the series, so the exact cluster structures were not clear. Nevertheless, Au_{13} NC typically showed an icosahedral structure with the possibility of a slight distortion of the

https://doi.org/10.1021/acs.jpcc.2c06370
J. Phys. Chem. C 2022, 126, 18374−18382

Au_{13} kernel.[37] The cluster structures of the series are subject to future studies.

Optical and Electrochemical Characterizations. Figure 3A displays the visible absorption spectrum of **4c** in DCM (the photoluminescence quantum yield needed to be compared in DCM with the literature, so optical characterizations were first performed in DCM). The characteristic ligand-to-metal charge-transfer (LMCT) transition[38] absorption peak was found at 420 nm with an absorption shoulder at around 490 nm. The absorption tailed down over 600 nm, covering a large portion of the visible spectrum. The photoluminescence (PL) spectrum of **4c** showed the maximum emission at 710 nm (Figure 3A). The large Stokes shift over 290 nm and the dissimilarity between the absorption and PL profiles indicated that the Au NC excited state is indeed a charge-separated state. **3a** and **4b** showed similar absorption and PL spectra to **4c** (Figure S2). The time-resolved PL of **4c** in DCM solution showed single exponential PL decay originating from LMCT[38] with a lifetime of 3.4 μs (Figure 3B). The PL quantum yield was determined using zinc phthalocyanine (ZnPc) as the standard according to the method reported before (Figure S3).[24] The quantum yield of **4c** was 56% after calculation, which was higher than those of **3a** and **4b** and most of the NHC-protected Au NCs reported up to now.[20,21,23,24]

With the experimentally determined quantum yield and τ, the radiative decay rate constant k_r and the nonradiative decay rate constant k_{nr} of **4c** can be obtained by eqs 2 and 3

$$\tau = \frac{1}{k_r + k_{nr}} \tag{2}$$

$$\mathrm{QY} = \frac{k_r}{k_r + k_{nr}} \tag{3}$$

The calculated results of k_r and k_{nr} of **3a**, **4b**, and **4c** are listed in Table 1. With the increasing chelating number and bulkiness of the ligands, the nonradiative transition was suppressed, and k_{nr} decreased following the order of **3a** > **4b** > **4c**, while k_r was similar across the series. The presence of pyrene-modified bidentate NHC ligands greatly increased the steric hindrance, hence significantly enhancing the $\pi-\pi$ and CH$-\pi$ interactions and the rigidity of the external ligands of **4c**.[20,39,40] The molecular structural rigidity helped minimize nonradiative decay and increase the quantum yield of **4c**.[41−43] Hence, **4c** obtained the highest photoluminescence quantum yield among the investigated Au NCs on account of the structural rigidity benefiting from both the chelating number and peripheral ligand steric hindrance.

Table 1. Photophysical Properties of Different Au NCs[a]

Au NC	τ_1 (μs)	QY (%)	k_r (s^{-1})	k_{nr} (s^{-1})	$E_{0,0}$ (eV)
3a	1.1	19	1.73×10^5	7.36×10^5	2.13
4b	2.6	38	1.46×10^5	2.38×10^5	2.11
4c	3.4	56	1.66×10^5	1.30×10^5	2.06

[a]Data were all measured in DCM.

The van der Waals interaction between the side groups of the bulky NHC to Au was much stronger than that of the less sterically bulky NHC to Au.[17] The ligands with larger NHC peripheral groups possessed more substantial structural rigidity, which could better protect the Au core and restrain vibrational relaxation. The restriction of vibration relaxation would lead to the improvement of the quantum yield. Therefore, the increase in structural stiffness was responsible for the increase in the quantum yield from **3a** to **4c**. The goal of improving the photoluminescence and lifetime was achieved through the NHC ligand design.

Differential pulse voltammetry (DPV) was carried out to determine the redox potentials of **4c** (Figure S4). The first oxidation peak (O1) was electrochemically reversible with $E^{ox}_{1/2}$ at 0.37 V, and the first reduction peak (R1) was not as clear as O1 due to the superposition of other reduction peaks. Nevertheless, it was estimated from the half-current peak height that $E^{red}_{1/2}$ was −1.57 V.

The NHC ligand-protected Au NCs were examined as photosensitizers for possible photoredox catalysis applications in which MV^{2+} was used as the model electron acceptor.[44] The Gibbs free energy change of electron transfer (ΔG) from **4c** to MV^{2+} was crudely estimated through the simplified Rehm−Weller equation (eq 4).[45]

$$\Delta G = e(E^{ox}_D - E^{red}_A) - E_{0,0} + C \tag{4}$$

where E^{ox}_D and E^{red}_A are the first one-electron oxidation of **4c** (0.37 V, Figure S4) and the reduction potential of MV^{2+} (−0.46 V vs SCE),[46] respectively, $E_{0,0}$ is the molecular zero−zero transition energy obtained from the intersection of the absorption and PL spectra ($E_{0,0}$ = 2.06 eV for **4c**), and C refers to the energy of the Coulombic interaction. The Coulombic term is usually so small in polar media that it can be ignored.[47]

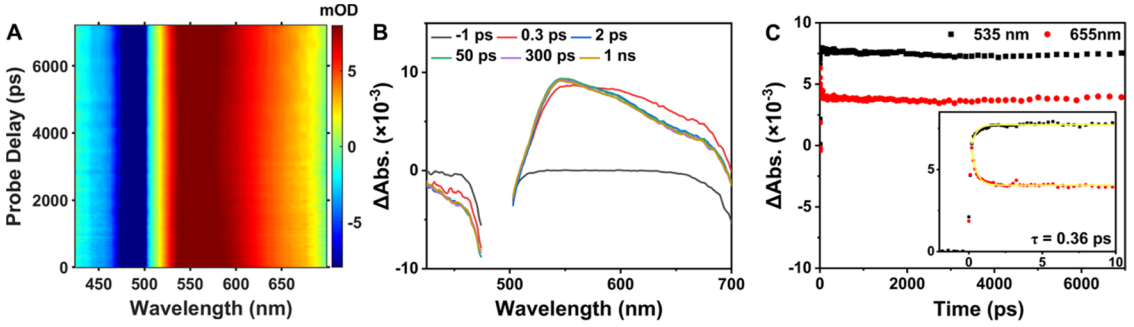

Figure 4. (A) Femtosecond transient absorption spectra of **4c** (contour plot). (B) fs-TA spectra of **4c** at room temperature in acetonitrile after 500 nm pulsed laser excitation at indicated delay times. (C) Kinetic trace curve of **4c** at 535 and 655 nm wavelength following the 500 nm laser pulse excitation. The inset shows the enlarged kinetic trace at early timescales. Overlaid in yellow is the single exponential fit to the kinetic data before 10 ps.

https://doi.org/10.1021/acs.jpcc.2c06370
J. Phys. Chem. C 2022, 126, 18374−18382

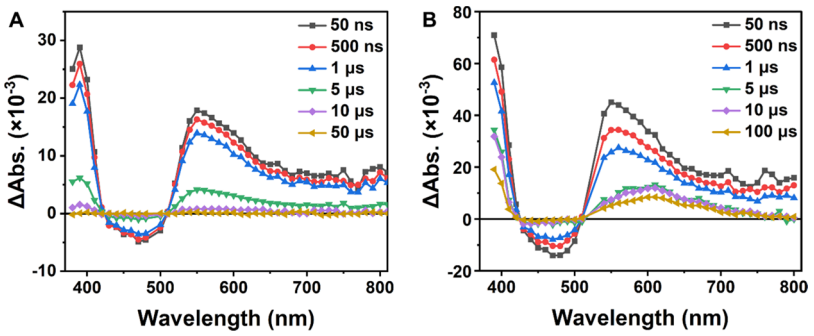

Figure 5. (A) Nanosecond transient absorption spectra of **4c** at room temperature in acetonitrile after 490 nm pulsed laser excitation at indicated delay times. (B) ns-TA spectra of **4c** in the presence of MV^{2+} in acetonitrile after 520 nm laser pulse excitation at indicated delay times.

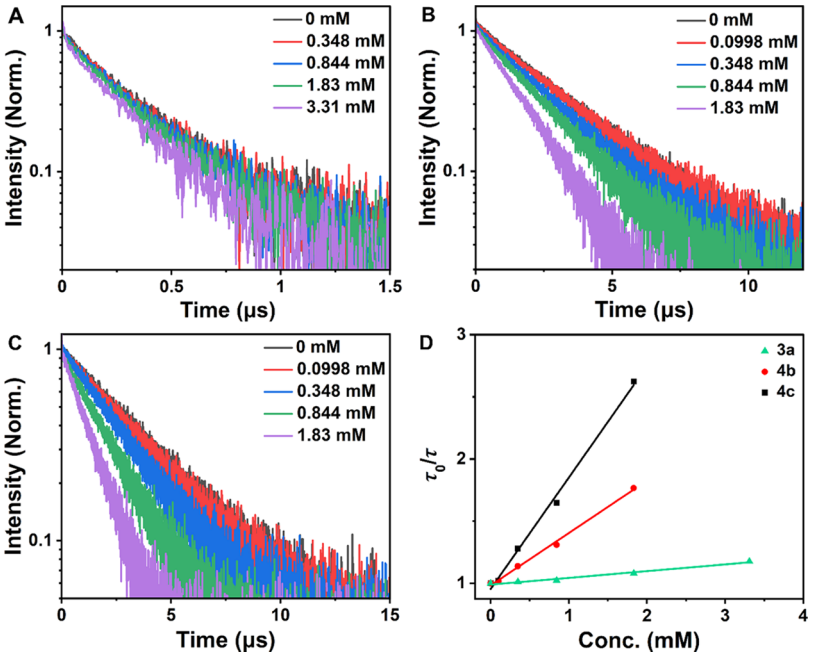

Figure 6. Time-resolved photoluminescence decay of (A) **3a**, (B) **4b**, and (C) **4c** with different MV^{2+} concentrations at probe wavelengths of 710 nm following photoexcitation at 490 nm in CH_3CN. (D) Stern−Volmer quenching plot of **3a**, **4b**, and **4c** with different concentrations of MV^{2+} in acetonitrile.

The ΔG was calculated to be −1.23 eV. The large negative ΔG indicated that electron transfer from the **4c** excited state to MV^{2+} was thermodynamically downhill.

Transient Kinetics and Dynamics of NHC-Stabilized Au NCs. Figure 4A displays the fs-TA spectra of **4c**. An excited-state absorption (ESA) band that peaked at around 550 nm and a ground-state bleach (GSB) band that peaked at around 480 nm are observed in Figure 4B. The single-wavelength kinetics of **4c** monitored at 535 and 655 nm indicated that there were two kinetic processes on the ultrafast timescale (Figure 4C). One was an ultrafast process with a single exponential decay time constant of 0.36 ps. The other was a long-lived process beyond the fs-TA time window (>8 ns). The 0.36 ps kinetic process can be attributed to the process from the MMCT excited state to the lowest-lying LMCT excited state.[38] For the fs-TA data of **3a** (Figure S5) and **4b** (Figure S6), they have similar results where two kinetic processes were observed on the ultrafast timescale. One was an ultrafast process with a single exponential decay time constant of 0.42 and 0.16 ps for **3a** and **4b**, respectively. The other was a long-lived process beyond the fs-TA time window (>8 ns).

The time-dependent transient absorption spectra were also quantified using global analysis and two excited-state species were observed (Figure S7). Species one was associated with a time constant of 0.05 ps, which was associated with large uncertainty as the time resolution of our fs-TA apparatus was around 0.15 ps. Species two was associated with a time constant beyond 8 ns. The global analysis for the ultrafast spectra of **4b** (Figure S8) is also shown in the Supporting Information.

Nanosecond transient absorption spectroscopy was carried out to gain insights into the excited-state electron transfer dynamics of Au NCs in acetonitrile solutions. Figure 5A shows the transient absorption spectra of **4c** in acetonitrile. Two ESA bands that peaked at 390 and 550 nm and a GSB band that peaked at 470 nm were observed. In addition, the preservation of clean isosbestic points in the nanosecond transient absorption spectra in Figure 5A also proved the excited state of only one species. The matching of the decay lifetime of the bleach recovery at 470 nm and absorption decay at 550 nm suggested the formation of a single transient species following the laser pulse excitation (Figure S9). The nanosecond

https://doi.org/10.1021/acs.jpcc.2c06370
J. Phys. Chem. C 2022, 126, 18374−18382

transient absorption lifetime data (3.2 μs, Figure S9) as well as the photoluminescence lifetime data (3.5 μs, Figure S10) both showed single exponential decay kinetics and corroborated well with each other. The ns-TA spectra of **3a** and **4b** are also shown in Figure S11. When MV^{2+} was added to the **4c** solution, the ns-TA spectra displayed several differences (Figure 5B). First, recovery of the bleach signal at 470 nm became much faster. Second, new absorption bands evolved in the UV and at 610 nm. The new bands were consistent with the one-electron reduced methyl viologen ($MV^{+\bullet}$) absorption reported at 397 and 607 nm.[48] The prolonged kinetics monitored at 400 nm showed charge recombination between $MV^{+\bullet}$ and $\mathbf{4c}^{+}$ through diffusional encounters, as shown in Figure S12.

Quantification of Excited-State Quenching and Electron Transfer. Stern−Volmer quenching experiments were conducted to access the Au NC excited states reactivity towards the MV^{2+} electron acceptor. The transient decay of Au NC PL recorded at 710 nm was found to decrease as the concentration of MV^{2+} increased (Figure 6A−C). The excited-state quenching of each Au NCs was followed by recording the time-resolved PL decay. Then, the obtained decay lifetime of the excited state at different MV^{2+} concentrations was fitted to the Stern−Volmer equation (eq 5).

$$\frac{\tau_0}{\tau} = K_{sv}[MV^{2+}] + 1 = k_q\tau_0[MV^{2+}] + 1 \quad (5)$$

where τ_0 is the observed lifetime of the Au NC excited state in the absence of quenchers, τ represents the observed lifetime of the excited state at different MV^{2+} concentrations, and K_{sv} is the Stern−Volmer constant. The second-order rate constant of diffusional electron transfer k_q is equal to K_{sv}/τ_0. The relationship between τ_0/τ and different concentrations of MV^{2+} was linear and fitted the Stern−Volmer equation well (Figure 6D). The k_q values obtained from the plot were 1.38×10^8, 1.50×10^8, and 2.53×10^8 M^{-1} s^{-1} for **3a**, **4b**, and **4c**, respectively. These second-order quenching constants were all about 2 orders of magnitude below the diffusion-limited rate constant in acetonitrile. Considering the large electron transfer driving force well above 1 eV, the bimolecular electron transfer reaction might fall into the Marcus inverted region and result in a decrease of the rate constants.

The quenching efficiency, Φ_q, was calculated using eq 6.

$$\Phi_q = \frac{k_q[MV^{2+}]}{k_q[MV^{2+}] + k_0} \times 100\% \quad (6)$$

where k_0 is the observed decay rate constant of the Au NC excited state in the absence of quenchers ($1/\tau_0$). The data on quenching efficiency are summarized in Table 2. Φ_q varied from 9.0 to 62%, with **4c** exhibiting the highest quenching efficiency. It might be counterintuitive to think that Au NCs with bulky ligands like the NHC with pendent pyrene would slow down electron transfer because of weaker electronic coupling between electron donors and acceptors, as predicted by the Marcus theory. However, we think the much longer excited-state lifetime of **4c** contributed the most to the high Φ_q.

Table 2. Quenching Rate Constants, Quenching Efficiency, and Photocatalytic Reduction Yield (η) for Different Au NCs[a]

cluster	τ_2 (μs)	k_0 (s^{-1})	k_q(M^{-1} s^{-1})	Φ_q (%)	Φ_{e-T} (%)	η (%)
3a	0.39	2.56×10^6	1.38×10^8	9.0	2.1	23
4b	2.8	3.56×10^5	1.50×10^8	43	3.9	9.1
4c	3.5	2.82×10^5	2.53×10^8	62	12	19

[a]Data were all measured in CH_3CN.

The following equations depict the electron transfer process from Au NCs to MV^{2+}. Au NCs were first excited to excited states after visible light absorption (eq 7). Part of the Au NC* went back to the ground state (eq 8-1), and the other participated in the electron transfer process from Au NC* to MV^{2+} (eq 8-2), which caused the charge-transfer (CT) state. Then, part of the CT state formed the separation state of $MV^{+\bullet}$ and Au NC^{+} (eq 9), and the other suffered a charge recombination to Au NC and MV^{2+} (eq 10).

$$\text{Au NC} + h\upsilon \rightarrow \text{Au NC}^* \quad (7)$$

$$\text{Au NC}^* \rightarrow \text{Au NC} \quad (8\text{-}1)$$

$$\text{Au NC}^* + MV^{2+} \rightarrow [\text{Au NC}^{+}\cdots MV^{+\bullet}] \quad (8\text{-}2)$$

$$[\text{Au NC}^{+}\cdots MV^{+\bullet}] \rightarrow \text{Au NC}^{+} + MV^{+\bullet} \quad (9)$$

$$[\text{Au NC}^{+}\cdots MV^{+\bullet}] \rightarrow \text{Au NC} + MV^{2+} \quad (10)$$

Quenching of Au NC excited states did not always result in charge-separated states. The electron transfer yield is only a fraction of the quenching yield. Yet sufficient yield for excited-state charge separation is critical for Au NCs to be used as photosensitizers in photoredox catalysis. To obtain the excited-state electron transfer quantum yield of Au NCs, the following experiments were carried out.[38,49] The triplet excited C_{60} ($^3C_{60}$*) in toluene was adopted as the actinometer; it was prepared to have the approximate absorbance as the Au NCs in acetonitrile at the laser excitation wavelength of 520 nm (Figure S13). Thenceforth, the peak of $^3C_{60}$* at 750 nm and $MV^{+\bullet}$ at 400 nm with different concentrations of MV^{2+} were detected. The absorption−time curves for **4c** at different concentrations of MV^{2+} are revealed in Figure 7A. Similar curves for **3a** and **4b** are presented in Figure S14. The average values from 10 to 15 μs where Au NC excited states completely decayed were selected to obtain the different absorption values to determine the concentration of $MV^{+\bullet}$. Then, the quantum efficiency of $MV^{+\bullet}$, Φ_{e-T}, was calculated according to eq 11.[49]

$$\Phi_{e-T} = \Phi_T \frac{A_{MV^{+\bullet}}\varepsilon_{C_{60}^*}}{A_{C_{60}^*}\varepsilon_{MV^{+\bullet}}} \times 100\% \quad (11)$$

where Φ_T is the quantum yield of $^3C_{60}$* (Φ_T = 1.0), $A_{C_{60}^*}$ and $A_{MV^{+\bullet}}$ are the maximum absorbance in the transient traces for the triplet excited state of $^3C_{60}$* (at 750 nm) and $MV^{+\bullet}$ (at 400 nm), and $\varepsilon_{C_{60}^*}$ and $\varepsilon_{MV^{+\bullet}}$ are the extinction coefficients of $^3C_{60}$* ($\varepsilon_{C_{60}^*}$ = 12 000 M^{-1} cm^{-1})[50] and $MV^{+\bullet}$ ($\varepsilon_{MV^{+\bullet}}$ = 41 800 M^{-1} cm^{-1})[51] at 750 and 400 nm in acetonitrile, respectively.

The quantum efficiency of electron transfer from Au NCs to MV^{2+} is illustrated in Figure 7B. With the increase of MV^{2+} concentration, the quantum efficiency of the reduction of MV^{2+} increased. The yields of electron transfer would reach their respective maximum values and remain unchanged when MV^{2+} arrived at a certain concentration. **4c** had the highest Φ_{e-T} among the investigated Au NCs. The observed high Φ_{e-T} of **4c** could be attributed to the long-lived excited state of **4c**

https://doi.org/10.1021/acs.jpcc.2c06370
J. Phys. Chem. C 2022, 126, 18374−18382

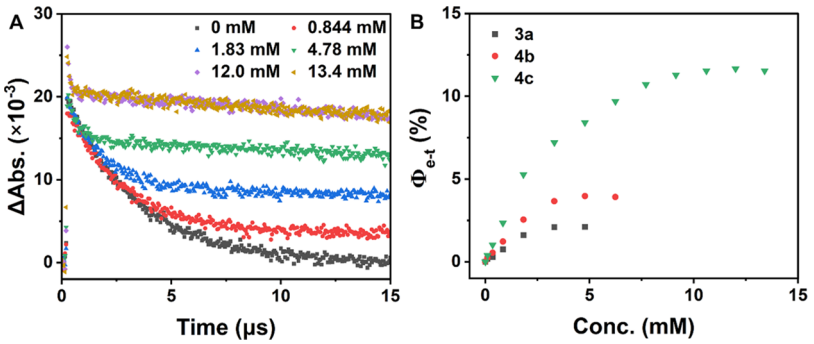

Figure 7. (A) Absorbance difference vs time curves recorded at 400 nm following 520 nm laser pulse excitation for **4c** in acetonitrile solution containing different MV^{2+} concentrations. (B) Quantum efficiency of electron transfer as a function of MV^{2+} concentration.

that ensures enough time for the excited state to reduce MV^{2+}. In comparison, the previous reports on electron transfer properties of gold nanoclusters to MV^{2+} mainly focused on GSH-Au NCs, and the net electron transfer efficiency was limited to 4.23% of that of $Au_{18}GSH_{14}$.[38,49,51] To the best of our knowledge, it is the first time to investigate Φ_{e-T} of NHC-stabilized Au NCs, and Φ_{e-T} of **4c** can reach up to 12%. The high efficiency enabled it to have high potential as a light-harvesting antenna. On account of the high electron transfer efficiency, coupled with the long PL quantum yield and the excited-state lifetime, **4c** is an excellent candidate as a visible light photosensitizer.

A series of other quenching parameters for electron transfer are listed in Table 2. Φ_q represents the total quenching efficiency. Higher Φ_q means more efficient photoluminescence quenching with MV^{2+}. Φ_{e-T} solely denotes the net electron transfer efficiency. Higher Φ_{e-T} refers to more efficient electron transfer with MV^{2+} out of total quenching.[38] The net excited-state electron transfer yield (η) is the ratio of the two efficiencies, Φ_{e-T}/Φ_q. The highest η of the Au NCs was of **3a**, while the highest Φ_{e-T} was obtained for **4c**. Back electron transfer still played a dominant role in the encounter complex since η was not close to unity. Nevertheless, the excited state of **4c** still represents the highest efficiency of electron transfer for Au NCs and has plenty of room to improve.

CONCLUSIONS

In conclusion, this study reported the synthesis of a series of Au NCs stabilized by NHC ligands with different chelating numbers and steric hindrances to prolong the photoluminescence lifetime. Their optical properties were studied in detail. The quantum yield and photoluminescence lifetime of Au NCs increased with the rising rigidity of NHC ligands, among which **4c** exhibited the highest quantum yield (56%) and the longest lifetime (3.4 μs, DCM). The excited-state properties of Au NCs played an essential role in determining photocatalytic activities. A strong correlation between the excited-state lifetime and photocatalytic activities was demonstrated during electron transfer to MV^{2+}. The photoactivity of Au NCs indicated that the photocatalytic reduction rate increased with increasing photoluminescence lifetime. Long-lived excited states, the high quantum yield, and the strong ability to participate in electron transfer suggested that **4c** could be a promising candidate as a photosensitizer for photoredox catalysis or solar energy harvesting.

ASSOCIATED CONTENT

Supporting Information

The Supporting Information is available free of charge at https://pubs.acs.org/doi/10.1021/acs.jpcc.2c06370.

Synthesis of NHC-stabilized Au NCs, experimental details, additional UV−vis spectra, photoluminescence spectra, femtosecond and nanosecond transient absorption spectra, and ^{1}H NMR spectra (PDF)

AUTHOR INFORMATION

Corresponding Author

Ke Hu − *Department of Chemistry and Shanghai Key Laboratory of Molecular Catalysis and Innovative Materials, Fudan University, Shanghai 200433, P. R. China;* orcid.org/0000-0002-0240-7192; Email: khu@fudan.edu.cn

Authors

Xiaotong Wang − *Department of Chemistry and Shanghai Key Laboratory of Molecular Catalysis and Innovative Materials, Fudan University, Shanghai 200433, P. R. China*

Rong Liu − *Department of Chemistry and Shanghai Key Laboratory of Molecular Catalysis and Innovative Materials, Fudan University, Shanghai 200433, P. R. China*

Limei Tian − *Department of Chemistry and Shanghai Key Laboratory of Molecular Catalysis and Innovative Materials, Fudan University, Shanghai 200433, P. R. China*

Jingwen Bao − *Anhui Province Key Laboratory of Optoelectronic Material Science and Technology, School of Physics and Electronic Information, Anhui Normal University, Wuhu 241002 Anhui, P. R. China*

Chunyi Zhao − *Anhui Province Key Laboratory of Optoelectronic Material Science and Technology, School of Physics and Electronic Information, Anhui Normal University, Wuhu 241002 Anhui, P. R. China*

Fushuang Niu − *Department of Chemistry and Shanghai Key Laboratory of Molecular Catalysis and Innovative Materials, Fudan University, Shanghai 200433, P. R. China*

Dajiao Cheng − *Department of Chemistry and Shanghai Key Laboratory of Molecular Catalysis and Innovative Materials, Fudan University, Shanghai 200433, P. R. China*

Zhou Lu − *Anhui Province Key Laboratory of Optoelectronic Material Science and Technology, School of Physics and Electronic Information, Anhui Normal University, Wuhu 241002 Anhui, P. R. China;* orcid.org/0000-0001-8527-0381

Complete contact information is available at:

https://doi.org/10.1021/acs.jpcc.2c06370
J. Phys. Chem. C 2022, 126, 18374−18382

https://pubs.acs.org/10.1021/acs.jpcc.2c06370

Notes

The authors declare no competing financial interest.

■ ACKNOWLEDGMENTS

The authors from Fudan University thank the National Natural Science Foundation of China (21872037) for financial support. The authors from Anhui Normal University are grateful for the financial support from the National Natural Science Foundation of China (22073001) and The University Synergy Innovation Program of Anhui Province (GXXT-2021-049).

■ REFERENCES

(1) Chakraborty, I.; Pradeep, T. Atomically Precise Clusters of Noble Metals: Emerging Link between Atoms and Nanoparticles. *Chem. Rev.* **2017**, *117*, 8208−8271.
(2) Liu, L.; Corma, A. Metal Catalysts for Heterogeneous Catalysis: From Single Atoms to Nanoclusters and Nanoparticles. *Chem. Rev.* **2018**, *118*, 4981−5079.
(3) Goswami, N.; Zheng, K.; Xie, J. Bio-NCs-the marriage of ultrasmall metal nanoclusters with biomolecules. *Nanoscale* **2014**, *6*, 13328−13347.
(4) Abbas, M. A.; Kamat, P. V.; Bang, J. H. Thiolated Gold Nanoclusters for Light Energy Conversion. *ACS Energy Lett.* **2018**, *3*, 840−854.
(5) Naldini, L.; Cariati, F.; Simonetta, G.; Malatesta, L. Gold-tertiary phosphine derivatives with intermetallic bonds. *Chem. Commun.* **1966**, *0*, 647−648.
(6) McPartlin, M.; Mason, R.; Malatesta, L. Novel cluster complexes of gold(0)-gold(I). *J. Chem. Soc. D* **1969**, *0*, 334.
(7) Kang, X.; Li, Y.; Zhu, M.; Jin, R. Atomically precise alloy nanoclusters: syntheses, structures, and properties. *Chem. Soc. Rev.* **2020**, *49*, 6443−6514.
(8) Yan, J.; Teo, B. K.; Zheng, N. Surface Chemistry of Atomically Precise Coinage-Metal Nanoclusters: From Structural Control to Surface Reactivity and Catalysis. *Acc. Chem. Res.* **2018**, *51*, 3084−3093.
(9) Lei, Z.; Wan, X.-K.; Yuan, S.-F.; Guan, Z.-J.; Wang, Q.-M. Alkynyl Approach toward the Protection of Metal Nanoclusters. *Acc. Chem. Res.* **2018**, *51*, 2465−2474.
(10) Konishi, K.Phosphine-Coordinated Pure-Gold Clusters: Diverse Geometrical Structures and Unique Optical Properties/Responses. In *Gold Clusters, Colloids and Nanoparticles I*; Mingos, D. M. P., Ed.; Springer International Publishing, 2014; pp 49−86.
(11) Kang, X.; Zhu, M. Transformation of Atomically Precise Nanoclusters by Ligand-Exchange. *Chem. Mater.* **2019**, *31*, 9939−9969.
(12) Gan, Z.; Xia, N.; Wu, Z. Discovery, Mechanism, and Application of Antigalvanic Reaction. *Acc. Chem. Res.* **2018**, *51*, 2774−2783.
(13) Li, S.; Tian, W.; Liu, Y. The ligand effect of atomically precise gold nanoclusters in tailoring catalytic properties. *Nanoscale* **2021**, *13*, 16847−16859.
(14) Liu, S.; Xu, Y. J. Photo-induced transformation process at gold clusters-semiconductor interface: Implications for the complexity of gold clusters-based photocatalysis. *Sci. Rep.* **2016**, *6*, No. 22742.
(15) Hopkinson, M. N.; Richter, C.; Schedler, M.; Glorius, F. An overview of N-heterocyclic carbenes. *Nature* **2014**, *510*, 485−496.
(16) Zhukhovitskiy, A. V.; MacLeod, M. J.; Johnson, J. A. Carbene Ligands in Surface Chemistry: From Stabilization of Discrete Elemental Allotropes to Modification of Nanoscale and Bulk Substrates. *Chem. Rev.* **2015**, *115*, 11503−11532.
(17) Tang, Q.; Jiang, D.-e. Comprehensive View of the Ligand-Gold Interface from First Principles. *Chem. Mater.* **2017**, *29*, 6908−6915.
(18) Tang, Q.; Hu, G.; Fung, V.; Jiang, D. E. Insights into Interfaces, Stability, Electronic Properties, and Catalytic Activities of Atomically Precise Metal Nanoclusters from First Principles. *Acc. Chem. Res.* **2018**, *51*, 2793−2802.
(19) Narouz, M. R.; Osten, K. M.; Unsworth, P. J.; Man, R. W. Y.; Salorinne, K.; Takano, S.; Tomihara, R.; Kaappa, S.; Malola, S.; Dinh, C. T.; et al. N-heterocyclic carbene-functionalized magic-number gold nanoclusters. *Nat. Chem.* **2019**, *11*, 419−425.
(20) Narouz, M. R.; Takano, S.; Lummis, P. A.; Levchenko, T. I.; Nazemi, A.; Kaappa, S.; Malola, S.; Yousefalizadeh, G.; Calhoun, L. A.; Stamplecoskie, K. G.; et al. Robust, Highly Luminescent Au_{13} Superatoms Protected by N-Heterocyclic Carbenes. *J. Am. Chem. Soc.* **2019**, *141*, 14997−15002.
(21) Shen, H.; Xiang, S.; Xu, Z.; Liu, C.; Li, X.; Sun, C.; Lin, S.; Teo, B. K.; Zheng, N. Superatomic Au_{13} clusters ligated by different N-heterocyclic carbenes and their ligand-dependent catalysis, photoluminescence, and proton sensitivity. *Nano. Res.* **2020**, *13*, 1908−1911.
(22) Hirano, K.; Takano, S.; Tsukuda, T. Ligand Effects on the Structures of $[Au_{23}L_6(C{\equiv}CPh)_9]^{2+}$ (L = N-Heterocyclic Carbene vs Phosphine) with Au_{17} Superatomic Cores. *J. Phys. Chem. C* **2021**, *125*, 9930−9936.
(23) Luo, P.; Bai, S.; Wang, X.; Zhao, J.; Yan, Z.-N.; Han, Y.-F.; Zang, S.-Q.; Mak, T. C. W. Tuning the Magic Sizes and Optical Properties of Atomically Precise Bidentate N-Heterocyclic Carbene-Protected Gold Nanoclusters via Subtle Change of N-Substituents. *Adv. Opt. Mater.* **2021**, *9*, No. 2001936.
(24) Yi, H.; Osten, K. M.; Levchenko, T. I.; Veinot, A. J.; Aramaki, Y.; Ooi, T.; Nambo, M.; Crudden, C. M. Synthesis and enantioseparation of chiral Au_{13} nanoclusters protected by bis-N-heterocyclic carbene ligands. *Chem. Sci.* **2021**, *12*, 10436−10440.
(25) Lummis, P. A.; Osten, K. M.; Levchenko, T. I.; Sabooni Asre Hazer, M.; Malola, S.; Owens-Baird, B.; Veinot, A. J.; Albright, E. L.; Schatte, G.; Takano, S.; et al. NHC-Stabilized Au_{10} Nanoclusters and Their Conversion to Au_{25} Nanoclusters. *JACS Au* **2022**, *2*, 875−885.
(26) Duan, M.; Hu, C.; Li, H.; Chen, Y.; Chen, R.; Gong, W.; Lu, Z.; Zhang, N.; Long, R.; Song, L.; Xiong, Y. Synergizing Inter and Intraband Transitions in Defective Tungsten Oxide for Efficient Photocatalytic Alcohol Dehydration to Alkenes. *JACS Au* **2022**, *2*, 1160−1168.
(27) Lu, X.; Tong, A.; Luo, D.; Jiang, F.; Wei, J.; Huang, Y.; Jiang, Z.; Lu, Z.; Ni, Y. Confining single Pt atoms from Pt clusters on multi-armed CdS for enhanced photocatalytic hydrogen evolution. *J. Mater. Chem. A* **2022**, *10*, 4594−4600.
(28) Cheng, D.; Liu, R.; Tian, L.; Zhou, Q.; Niu, F.; Yue, Y.; Hu, K. Photocatalytic Nitroaromatic Prodrug Activation by Functionalized Gold Nanoclusters. *ACS Appl. Nano Mater.* **2021**, *4*, 13413−13424.
(29) Yang, L.; Cheng, H.; Jiang, Y.; Huang, T.; Bao, J.; Sun, Z.; Jiang, Z.; Ma, J.; Sun, F.; Liu, Q.; et al. In situ studies on controlling an atomically-accurate formation process of gold nanoclusters. *Nanoscale* **2015**, *7*, 14452−14459.
(30) Parker, C. A.; Rees, W. T. Correction of fluorescence spectra and measurement of fluorescence quantum efficiency. *Analyst* **1960**, *85*, 587−600.
(31) Crosby, G. A.; Demas, J. N. Measurement of photoluminescence quantum yields. Review. *J. Phys. Chem. A* **1971**, *75*, 991−1024.
(32) Williams, A. T. R.; Winfield, S. A.; Miller, J. N. Relative fluorescence quantum yields using a computer-controlled luminescence spectrometer. *Analyst* **1983**, *108*, 1067−1071.
(33) Eaton, D. F. Reference materials for fluorescence measurement. *Pure Appl. Chem.* **1988**, *60*, 1107−1114.
(34) Fery-Forgues, S.; Lavabre, D. Are Fluorescence Quantum Yields So Tricky to Measure? A Demonstration Using Familiar Stationery Products. *J. Chem. Educ.* **1999**, *76*, 1260.
(35) Lide, D. R.*CRC Handbook of Chemistry and Physics*; CRC Press: Boca Raton, FL, 2005.
(36) Seybold, P. G.; Gouterman, M. Porphyrins: XIII: Fluorescence spectra and quantum yields. *J. Mol. Spectrosc.* **1969**, *31*, 1−13.

(37) Tlahuice-Flores, A.; Whetten, R. L.; Jose-Yacaman, M. Ligand Effects on the Structure and the Electronic Optical Properties of Anionic $Au_{25}(SR)_{18}$ Clusters. *J. Phys. Chem. C* **2013**, *117*, 20867−20875.
(38) Stamplecoskie, K. G.; Kamat, P. V. Size-dependent excited state behavior of glutathione-capped gold clusters and their light-harvesting capacity. *J. Am. Chem. Soc.* **2014**, *136*, 11093−11099.
(39) Ito, S.; Takano, S.; Tsukuda, T. Alkynyl-Protected $Au_{22}(C{\equiv}CR)_{18}$ Clusters Featuring New Interfacial Motifs and R-Dependent Photoluminescence. *J. Phys. Chem. Lett.* **2019**, *10*, 6892−6896.
(40) Takano, S.; Tsukuda, T. Chemically Modified Gold/Silver Superatoms as Artificial Elements at Nanoscale: Design Principles and Synthesis Challenges. *J. Am. Chem. Soc.* **2021**, *143*, 1683−1698.
(41) Li, Q.; Zeman, C. J. t.; Schatz, G. C.; Gu, X. W. Source of Bright Near-Infrared Luminescence in Gold Nanoclusters. *ACS Nano* **2021**, *15*, 16095−16105.
(42) Li, Q.; Zhou, M.; So, W. Y.; Huang, J.; Li, M.; Kauffman, D. R.; Cotlet, M.; Higaki, T.; Peteanu, L. A.; Shao, Z.; Jin, R. A Mono-cuboctahedral Series of Gold Nanoclusters: Photoluminescence Origin, Large Enhancement, Wide Tunability, and Structure−Property Correlation. *J. Am. Chem. Soc.* **2019**, *141*, 5314−5325.
(43) Chen, Y.; Zhou, M.; Li, Q.; Gronlund, H.; Jin, R. Isomerization-induced enhancement of luminescence in $Au_{28}(SR)_{20}$ nanoclusters. *Chem. Sci.* **2020**, *11*, 8176−8183.
(44) Peon, J.; Tan, X.; Hoerner, J. D.; Xia, C.; Luk, Y. F.; Kohler, B. Excited State Dynamics of Methyl Viologen. Ultrafast Photoreduction in Methanol and Fluorescence in Acetonitrile. *J. Phys. Chem. A* **2001**, *105*, 5768−5777.
(45) Rehm, D.; Weller, A. Kinetics of Fluorescence Quenching by Electron and H-Atom Transfer. *Isr. J. Chem.* **1970**, *8*, 259−271.
(46) Bock, C. R.; Connor, J. A.; Gutierrez, A. R.; Meyer, T. J.; Whitten, D. G.; Sullivan, B. P.; Nagle, J. K. Estimation of excited-state redox potentials by electron-transfer quenching. Application of electron-transfer theory to excited-state redox processes. *J. Am. Chem. Soc.* **1979**, *101*, 4815−4824.
(47) Sutin, N. Nuclear, electronic, and frequency factors in electron transfer reactions. *Acc. Chem. Res.* **1982**, *15*, 275−282.
(48) Watanabe, T.; Honda, K. Measurement of the extinction coefficient of the methyl viologen cation radical and the efficiency of its formation by semiconductor photocatalysis. *J. Phys. Chem. B* **1982**, *86*, 2617−2619.
(49) Stamplecoskie, K. G.; Chen, Y.-S.; Kamat, P. V. Excited-State Behavior of Luminescent Glutathione-Protected Gold Clusters. *J. Phys. Chem. C* **2014**, *118*, 1370−1376.
(50) Dimitrijevic, N. M.; Kamat, P. V. Triplet excited state behavior of fullerenes: pulse radiolysis and laser flash photolysis of fullerenes (C_{60} and C_{70}) in benzene. *J. Phys. Chem. C* **1992**, *96*, 4811−4814.
(51) Chatterjee, A.; Purkayastha, P. The impact of lipid head-groups in GUVs on electron transfer by surface-adsorbed fluorescent gold nanoclusters. *Mater. Adv.* **2021**, *2*, 1343−1350.

https://doi.org/10.1021/acs.jpcc.2c06370
J. Phys. Chem. C 2022, 126, 18374−18382